Wavefront-corrected XUV and soft X-ray spectroscopy

JÜRGEN PROBST[1], HEIKE LÖCHEL[1], CHRISTOPH BRAIG[2,*], ENRICO LANGLOTZ[3], ILKO RAHNEBERG[3], MICHAEL KÜHNEL[3], THOMAS ZESCHKE[4], FRANK SIEWERT[4], THOMAS KRIST[1], AND ALEXEI ERKO[2,4]

[1] NOB Nano Optics Berlin GmbH, Krumme Straße 64, 10627 Berlin, Germany
[2] Institute of Applied Photonics e.V., Rudower Chaussee 29/31, 12489 Berlin, Germany
[3] SIOS Meßtechnik GmbH, Am Vogelherd 46, 98693 Ilmenau, Germany
[4] Department for Nanometer Optics and Technology, Helmholtz-Zentrum für Materialien und Energie, Albert-Einstein-Str. 15, 12489 Berlin, Germany
[*] Corresponding author: braig@iap-adlershof.de

Compiled November 22, 2019

We present a simple and precise method to minimize aberrations of mirror-based, wavelength-dispersive spectrometers for the extreme ultraviolet (XUV) and soft X-ray range. The concept enables an enhanced resolving power $E/\Delta E$ over a wide spectral band with high efficiency, in particular close to the diffraction limit around the design energy of the instrument. Our optical element, the "diffractive wavefront corrector" (DWC), is individually shaped to the form and figure error of the mirror profile and can be fabricated by existing technologies on plane and even strongly curved substrates. Theory, simulations of various configurations like Hettrick-Underwood or compact all-in-one setups for TiO_2 spectroscopy with $E/\Delta E \lesssim 4.5 \times 10^4$, and aspects of their experimental realization are addressed.

OCIS codes: (050.1970) Diffractive optics; (050.6875) three-dimensional fabrication; (100.5070) phase retrieval; (120.6650) surface measurements, figure; (220.1000) aberration compensation; (300.6560) spectroscopy, x-ray; (340.7470) x-ray mirrors.

http://dx.doi.org/10.1364/ao.XX.XXXXXX

1. INTRODUCTION

Modern wavelength-dispersive spectroscopy for extreme ultraviolet (XUV) radiation and soft X-rays with photon energies between about 0.05 keV and 2 keV is typically based on a collecting mirror in combination with a varied-line-space (VLS) grating [1]. If well designed [2], they both together reduce geometrical and chromatic imaging errors in the convenient flat-field detection mode over a large spectral range of several 10 % of the design energy. In general however, the widely used since inexpensive toroidal mirror profile still introduces wavefront distortions – firstly, due to its deviation from the ideal ellipsoid and secondly, because of imperfect fabrication that becomes inevitably evident in a rough and bumpy surface [3].

For several years, correction mechanisms to improve the quality of reflective and other X-ray optics toward the ultimate resolution limit [4–6] are being intensively discussed. Until now, mainly mirrors applied in the hard X-ray regime or one-dimensional (1D) focusing systems have been corrected, either by additionally coated multilayers [7], using active X-ray optics [8, 9], or with refractive phase plates [10, 11]. The former approach requires a serious technical effort, whereas the latter method is excluded for radiation below 1 keV because of the absorption for all practical materials like e.g. SiO_2 or SU-8. Hence, there exists a strong need for beam shaping components [12, 13] being suitable for the XUV and soft X-ray range.

In this work, we propose the "diffractive wavefront corrector" (DWC) as a novel optical element that compensates for the phase deformations as induced by the erroneous mirror shape. The device can be understood as a generalized version of the well-known reflection zone plate (RZP) [14, 15] with its elliptical grooves to free-form 2D VLS gratings on fairly plane or irregularly curved substrates.

We choose a heuristic approach in Sect. 2 and correct an existing type of instrument by replacing the conventional 2D VLS grating by a customized DWC. The open question that remains, i.e. how to retrieve the phase whose accurate knowledge the adequate calculation and function of the DWC depends on, is addressed in Sect. 3. Equipped with that information on the wavefront, we are ready to integrate the overall arrangement and inscribe the DWC into the mirror surface – whose profile can be also measured directly as described in Sect. 4. The variety of experimental and theoretical ways to diffractive wavefront correction opens the door to further optics development and future-oriented X-ray science, as concluded in Sect. 5.

2. THE HETTRICK-UNDERWOOD SCHEME

We start with the instrumental configuration of an X-ray spectrometer, commonly used at synchrotron or X-ray laser facilities but also in laboratory-scaled, table-top experiments. Named after their inventors M. C. Hettrick and J. H. Underwood [1], we abbreviate the setup, visualized in Fig. 1, by "HU". For photons emitted from the source (S), the arrangement is composed of a

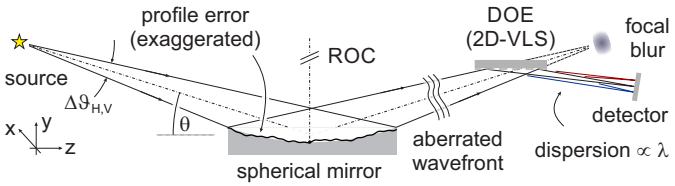

Fig. 1. Scheme of an X-ray HU spectrometer. The pre-focusing mirror with its radius of curvature (ROC) is followed by a 1D or 2D VLS grating that enables dispersion. In its optimized version, the diffractive optical element (DOE) compensates the mirror-introduced aberrations around the design wavelength.

collecting mirror (M) operated under total external reflection at an angle θ and a subsequent, fixed VLS grating (G) on a plane substrate. We assume separations $\overline{\mathrm{U}-\mathrm{V}}$ and angles as listed in Tab. 1, where E_0 represents the design energy. The parameters

Table 1. Design parameters of the example HU instrument

E_0	$\overline{\mathrm{S}-\mathrm{M}}$	ROC	θ	$\overline{\mathrm{M}-\mathrm{G}}$	α	β	$\overline{\mathrm{G}-\mathrm{D}}$
183 eV	0.4 m	8.6 m	4°	0.2 m	4°	8°	1.0 m

are adapted to the specific beamline properties or scientific demands, to create a flat-field spectrum on an imaging detector (D), e.g. CCD or CMOS array. The mirror's surface profile can be described as a perturbed sphere,

$$y_M(x,z) = y_{\mathrm{Form}}(x,z) + \delta y_{\mathrm{Fig.}}(x,z), \qquad (1)$$

where the first term describes the nominal "form" – a sphere in our case, with its deviation from the ideal ellipsoid, and the second one the irregular, relatively small "figure error". Since

$$y_{\mathrm{Form}}(x,z) = R_M - \sqrt{R_M^2 - x^2 - z^2} \quad \gg \quad \delta y_{\mathrm{Fig.}}(x,z), \qquad (2)$$

the profile function in Eq. (1) decouples second order distortions from y_{Form} that dominates the overall design via the ROC R_M. For our proof-of-principle simulation, we map measured [9] fabrication tolerances $\{x_i, y_i, z_i\}$ on the mirror's aperture as shown in Fig. 2. The grid spacing of these 3D data near 0.6 mm

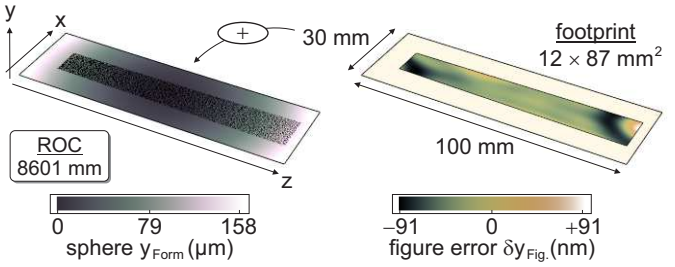

Fig. 2. Mirror substrate with its color-coded spherical form, characterized by the ROC, on the left and the additive figure error on the right. The black dots represent the rays' footprint of the incident beam. Note the different (P-V) amplitudes.

and the Nyquist-Shannon sampling theorem ensure a power spectral density (PSD) which mainly contains the relevant low spatial frequencies ($\lesssim 10^{-3}\,\mathrm{mm}^{-1}$). The nonlinear fit with a 2D polynomial of sufficiently high order P,

$$y_M(x,z) \approx \sum_{m=0}^{P} \sum_{n=0}^{P-m} c_{mn} x^m z^n \quad \text{with} \quad P = 16, \qquad (3)$$

and coefficients $c_{mn} \in \mathbb{R}$ provides an analytical, differentiable approximation to the mirror's surface on a confidence level of 95 %. Now we simulate an incomplete setup in the sequential Monte-Carlo mode: A monochromatic point source at $\vec{r}_{\mathrm{src.}}$ illuminates the mirror, as given by Eq. (3), uniformly. From there, the rays are reflected toward the grating substrate, which can be modeled as any planar optical element, e.g. an absorbing screen.

A. The optical path length method

For each individual ray indexed by the superscript (i), its total length OL_i (which equals the optical length in vacuum) is written with the Euclidian norm $\|.\|$ as the sum

$$\mathrm{OL}_i = \|\vec{r}_{\mathrm{src.}} - \vec{r}^{(i)}_{\mathrm{mir.}}\| + \|\vec{r}^{(i)}_{\mathrm{grat.}} - \vec{r}^{(i)}_{\mathrm{mir.}}\| + \|\vec{r}^{(i)}_{\mathrm{det.}} - \vec{r}^{(i)}_{\mathrm{grat.}}\|, \qquad (4)$$

where the 3D coordinates in the global system from Fig. 1 refer to the intersection points of the rays with the respective optical elements. In particular, $\vec{r}^{(i)}_{\mathrm{det.}}$ is not determined in the simulation but rather user-defined, according to the desired image type – in our case a "telescopic" line focus with $x^{(i)}_{\mathrm{det.}} \equiv x^{(i)}_{\mathrm{grat.}}\ \forall\, i$. Using Eq. (4) and the on-axis distance notation from Tab. 1, we obtain

$$\mathrm{OPD}(\tilde{x}^{(i)}_{\mathrm{grat.}}, \tilde{z}^{(i)}_{\mathrm{grat.}}) \equiv \mathrm{OL}_i - \left(\overline{\mathrm{S}-\mathrm{M}} + \overline{\mathrm{M}-\mathrm{G}} + \overline{\mathrm{G}-\mathrm{D}}\right), \qquad (5)$$

called the "optical path difference". Notably, the OPD is measured as a scalar function of the local 2D coordinates $\tilde{x}^{(i)}_{\mathrm{grat.}}, \tilde{z}^{(i)}_{\mathrm{grat.}}$ in the grating's substrate plane. The discrete data set is fitted once again conveniently with a 2D polynomial analog to Eq. (3). Figure 3 visualizes on the left the result of that semi-analytical procedure. If normalized to the design wavelength λ_0, the point-

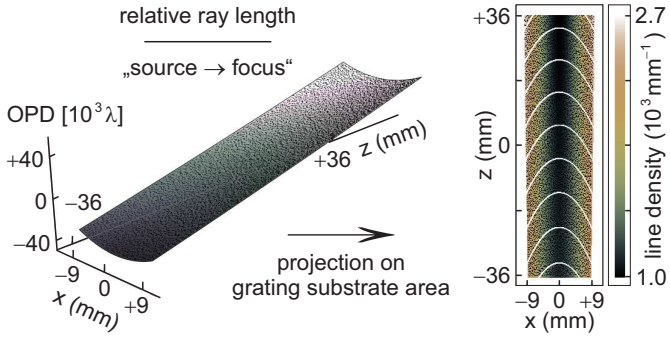

Fig. 3. Optical path length from source to detector, relative to the length of the principal ray, across the grating area on the left and the corresponding groove structure of the DWC on the right. Black dots indicate traced rays from the simulation.

wise deviation of the ray-traced data according to Eq. (5) from the OPD fit function measures the residual phase error which will affect the subsequent wavefront correction. The sample mirror from Fig. 2 is approximated at best to an accuracy of about $\pm\lambda_0/1200$ (rms) for instance, usually considered as sufficiently precise for diffraction-limited imaging. Despite such inaccuracies, the fit allows us to treat the system analytically, rather than by interpolation. In the final step to design the DWC, we project the phase Φ similar to a hologram onto the grating substrate via $\Phi(\tilde{x}_{\mathrm{grat.}}, \tilde{z}_{\mathrm{grat.}}) = 2\pi\lambda_0^{-1}\mathrm{OPD}(\tilde{x}_{\mathrm{grat.}}, \tilde{z}_{\mathrm{grat.}})$ and apply the "Fresnel zone equation" for a binary structure,

$$\Phi(\tilde{x}_{\mathrm{grat.}}, \tilde{z}_{\mathrm{grat.}}) = m \cdot \pi \quad \text{for} \quad m \in \mathbb{Z}. \qquad (6)$$

The implicit Eq. (6) is solved for the m^{th} Fresnel zone $\tilde{z}_m(\tilde{x})$ – the index "grat." has been omitted for simplicity – using an appropriate computer algorithm. Figure 3 depicts on the right the shape of representative grating lines. Their apparent similarity to grooves of a regular RZP with elliptical zones deceives: To prove the effect of the μm-scaled deviations, we derive [16] via

$$2\pi\vec{g}(\tilde{x}_{\text{grat.}},\tilde{z}_{\text{grat.}}) = \vec{\nabla}_{\tilde{x}_{\text{grat.}},\tilde{z}_{\text{grat.}}} \cdot \Phi(\tilde{x}_{\text{grat.}},\tilde{z}_{\text{grat.}}) \qquad (7)$$

the vector field $\vec{g}(\tilde{x}_{\text{grat.}},\tilde{z}_{\text{grat.}})$, identify it with the 2D line density and simulate the focusing capabilities of the DWC in a feedback loop by ray tracing. Figure 4 compares its performance to that of an uncorrected, ordinary RZP in the same optical setup from Fig. 1. The DWC effect over a wide spectral range

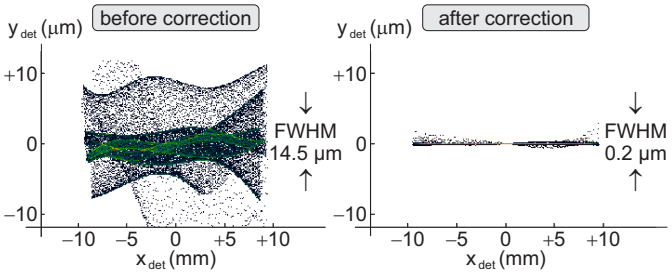

Fig. 4. Aberrations in the detector plane before (left) and after (right) correction, simulated for the focal line at the design energy of 183 eV. End points of traced rays appear as black dots or – in case of high intensity – as a color-encoded distribution.

is evaluated for a test spectrum with photon energies from 147 eV to 237 eV, which disperse over $\approx$ 25 mm in the detection plane. Assuming perfect alignment and neglecting practical restrictions such as the finite source or pixel size, aberrations constrain the resolving power $E/\Delta E$ to $\mathcal{R}(E_0) = 6.7 \times 10^4$, about 13 % below the natural diffraction limit which is given by the number of illuminated grating lines. In Fig. 5, the simulated data follow a modified model [17] for RZP-based spectrometers, $\mathcal{R}(E) = [1 + [\sigma_0^{-1}(E - E_0)]^2]^{-1/2}\mathcal{R}(E_0) + \sigma_\infty^{-1}(E - E_0)$ with $\sigma_0 \approx 0.53$ and $\sigma_\infty \approx 0.34$. The resolving power ratio to the

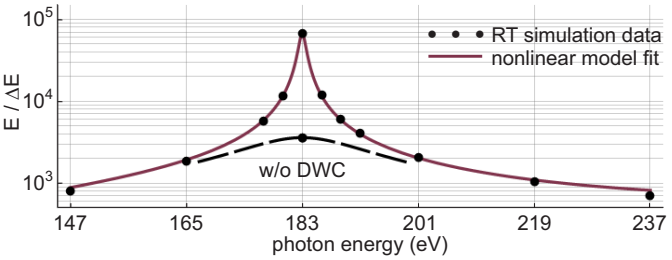

Fig. 5. Resolving power of the HU spectrometer from Fig. 1 for a coherent source. Simulation results (dots) are fitted [17] (red curve), and the performance of an ordinary RZP is sketched by means of a black, dashed line. Far from the design energy, i.e. for $|E - E_0| \gtrsim 18$ eV, both curves nearly coincide.

uncorrected version peaks sharply at E_0 but degrades asymptotically to $\gtrsim 1$ for off-design X-ray energies, where the spherical form dominates, $y_{\text{Form}}(x,z) \ggg \delta y_{\text{Fig.}}(x,z)$, according to Fig. 2.

B. The line density approach

An alternative strategy to the direct use of the OPD determines at first the vector field $\vec{g} = (g_x, g_z)$ of the line density at the local substrate position $(\tilde{x},\tilde{z})$, again without the index "grat.", from

- the **grating equation** in its general [18], two-dimensional form with partially conical diffraction for the incident beam;
- the **focusing condition** at the design energy, e.g. to a line or point focus [16], for the outgoing beam toward the detector.

Specialized simulation software such as RAY-UI [19] is capable to scan that 2D line density on a matrix-like grid across the aperture of the DWC being designed. By means of high-order polynomials, either in the standard form as defined in Eq. (3) or using Legendre polynomials in 2D as an orthogonal basis [20], these data may be subsequently fitted again, to obtain the continuous, differentiable function $\vec{g}(\tilde{x},\tilde{z})$. The term

$$(2\pi)^{-1}\Phi(\tilde{x},\tilde{z}) \approx \int g_z(\tilde{x},\tilde{z})dz + \int \mathcal{F}(\tilde{x},\tilde{z})dx \qquad (8)$$

defines a path integral in the DWC area, that yields the phase $\Phi(\tilde{x},\tilde{z})$ again. In the auxiliary function as used in Eq. (8),

$$\mathcal{F}(\tilde{x},\tilde{z}) \equiv g_x(\tilde{x},\tilde{z}) - \partial_x \int g_z(\tilde{x},\tilde{z})dz, \qquad (9)$$

the partial derivative ∂_x acts on the following integral over dz.

An optical setup proposed for resonant inelastic X-ray scattering (RIXS) around 150 eV [21], in fact very similar to the configuration as specified in Tab. 1, is chosen to demonstrate the functionality: Figure 6 illustrates the correspondence between an – in the present case – simulated figure error profile and the associated DWC, integrated from $\vec{g}(\tilde{x},\tilde{z})$ and applying Eq. (6). The result should be subject to a control loop via Eq. (7). The

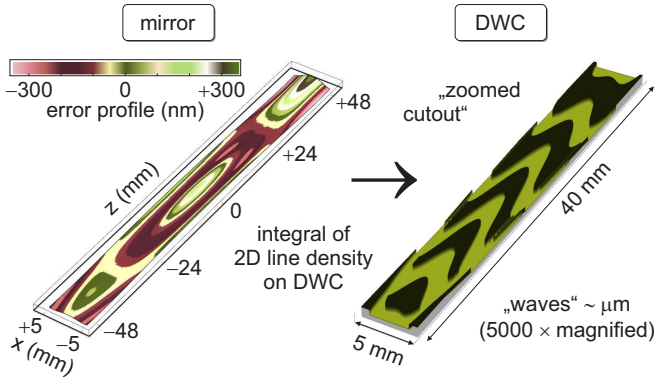

Fig. 6. Simulated deformation of a spherical mirror (left) and its diffractive correction (right) in a HU system, calculated via $\vec{g}(\tilde{x},\tilde{z})$ and displayed on a cut region of the full size $\sim (10^1 \times 10^2)$ mm^2. Note that the "wavy" line characteristic is artificially enhanced for illustrative purposes – in reality, the grooves deviate on a scale of a few μm from straight horizontal lines.

relative deviations between the grating vector field which is derived as the gradient of the phase from Eq. (8) and its original $\vec{g}(\tilde{x},\tilde{z})$ are typically negligible for the lateral component g_x, here in the order of 10^{-13} %. In the critical, axial dimension in contrast, the line density differs by $\sim 10^{-2}$ %. The precision of the DWC structures as calculated by means of that integration method falls therefore short of those which follow from the OPD, using Eq. (6). The errors are, according to the present state of knowledge, however tolerable and the amplitudes of the focal aberrations in the order of $\approx (0.33 \pm 0.13)$ μm (FWHM) lie below the practical detection limit, which is e.g. constrained by the spatial detector resolution of usually at least a few μm.

Besides, there's a way to circumvent the phase at all. We make use of the discrete 2D line density data scanned across the grating aperture once more, as described above. On the one hand, the local slope of the grating lines results from the quotient g_x/g_z. Compared to the separate fit of both vector components, the simplified single fit of their ratio tends to diminish the residual wavefront error. On the other hand, the axial component $g_z(0,\tilde{z})$ yields the groove distribution $\tilde{z}_m^{(0)}$ for $m \epsilon \mathbb{Z}$ via 1D integration along $\tilde{z}$ immediately. These values serve as initial conditions for the iterative, approximative solution of the ordinary differential equation

$$\frac{d}{dx}\tilde{z}_m(\tilde{x}) \approx \pm\frac{g_x[\mp\tilde{x},\tilde{z}_m(\tilde{x})]}{g_z[\mp\tilde{x},\tilde{z}_m(\tilde{x})]} \quad \text{with} \quad \tilde{z}_m(0) \equiv \tilde{z}_m^{(0)} \qquad \textbf{(10)}$$

by the established "Runge-Kutta" method, for instance. The reliable algorithm needs to maintain the stability as far as possible, to avoid an addition of numerical errors, namely the gradual deviation of the curve $\tilde{z}_m(\tilde{x})$ from its exact shape. Hence, this method works best in the case of relatively straight grooves with an only weak slope $d\tilde{z}_m(\tilde{x})/dx$, similar to a 1D VLS grating. A further enhancement of the numerical precision is achieved via balancing the numerically small, axial asymmetries to the final result $\langle\tilde{z}_m(\tilde{x})\rangle_\pm$ for the sign cases in Eq. (10).

Both mathematical techniques, the integration of the 2D line density and its interpretation as a vector field in the differential equation, lead to nearly identical solutions. For the example studied here in Sect. B, we compute the mean deviation $\langle\delta\tilde{z}_m(\tilde{x})\rangle_{x,m}$ between grating lines of the same number m, being calculated by the two methods. Across the full aperture of the DWC, that error amounts to no more than (0.36 ± 0.23) nm – negligible in comparison to the mean period of 1.67 μm, which corresponds to a residual, maximum wavefront error of $\lesssim \lambda/3 \times 10^3$.

Using RAY-UI, the HU spectrometer [21] which is now equipped with the DWC from Fig. 6 instead of the original 1D VLS grating, is "traced" again. The straight focal line, that covers nearly the full CCD (27.6 mm) in its width, shows tiny rest aberrations with an overall FWHM of only 0.4 μm in the dispersive direction – well below the uncorrected spatial resolution of 20 μm and even still less than the diffraction limit of 1.2 μm.

3. ABERRATION ANALYSIS VIA PHASE RETRIEVAL

With the successfully corrected profile distortions in Sect. 2, one question remains: How to unveil the wavefront that carries the footprint of $y_M(z)$ in terms of the spatial phase distribution along the propagating beam? Among others [22–25], one popular method is based upon a measurement of the 3D intensity distribution in the focal vicinity, evaluated by CCD recordings in at least 2 detection planes at different distance from the mirror. Figure 7 shows the principle of the technique. Our experiment is performed as follows. The available electron source (4.4 keV, max. 10 μA) is assumed to excite an emission region of 7 μm in diameter (FWHM) on the Carbon target. Kα fluorescence at 277 eV is generated predominantly, accompanied by weak bremsstrahlung with an intensity $(3-4)$ orders of magnitude below the Kα peak [26].

A commercially available [27], spherical mirror sample "M_1" is studied, with parameters as listed in Tab. 2. Mounted on the 6-axis goniometer "SmarPod 225.75" (SmarAct GmbH), the mirror can be adjusted with nm/μrad precision. Illuminated from a distance $R_1' = 838$ mm under the grazing incidence angle $\theta = 1.65°$, the mirror reflects (74.72 ± 0.02) % of the unpolarized X-rays to a horizontally divergent, nearly straight focal line

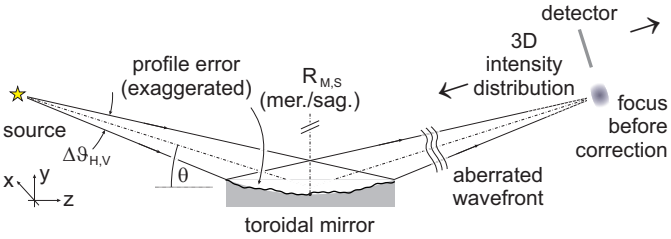

Fig. 7. *In situ* phase measurement with a nearly point-like, i.e. in part spatially coherent source. The imaging detector is stepwise moved along the optical axis to retrieve the 3D intensity distribution in the vicinity of the aberrated focus.

Table 2. Technical specifications of the mirror sample "M_1"

size $(L \times W)$	$\Delta t_{\text{sub.}}$	ROC	surface	$\pm\sigma$ (rms)
$120 \times 30\,\text{mm}^2$	8 mm	29.13 m	blank Si	≈ 0.25 nm

at a distance $R_2' = R_1'$ in the symmetric configuration. The CCD camera (Andor, "CCD 47-10"), which resolves structures with an effective pixel size of $\approx 25\,\mu$m due to electronic split events, is moved to 7 positions in- and outward of the focal plane, recording the series of intensity patterns in Fig. 8. The integration time of 30 s for all exposures (except from the 0.5 s for the focal line image at $R_2' = 838$ mm) and a low dark count rate of $\approx 20\,\text{s}^{-1}$ ensure a sufficiently high signal-to-noise ratio.

We compare the experimental outcomes with simulations using the partially known mirror profile: The proven and reliable metrology technique [28, 29] based on the long trace profiler (LTP) probes the tangential, local slope along the central, on-axis surface line of the mirror on a length of 100 mm. The numerical integration of these data yields the absolute, 1D height profile $y_M(z)$ as introduced in Eq. (1) with an error amplitude $\delta y_{\text{Fig.}}(z) = \pm 31$ nm (P-V) or $\langle\delta y_{\text{Fig.}}\rangle_z = \pm 20$ nm (rms). As displayed in Fig. 8, the thereby obtained ray tracing results coincide well with the intensity measurements, verifying their correctness within $-50\,\text{mm} \le y \le +50\,\text{mm}$.

For the subsequent wavefront reconstruction, either an iterative algorithm [30] in analogy to the Gerchberg-Saxton code or the deterministic approach [31] via the transport-of-intensity equation (TIE) may be used. Based on the latter option [32] in accordance with the instrumental conditions of – to a far extent – incoherent light and an only small number of detection planes, we apply here an elementary and particularly robust procedure. The TIE, which simplifies in our case of the 1D intensity profile $I(y,z)$ and its associated phase $\Phi(y,z)$ to

$$-2\pi\lambda_0^{-1}\partial_z I(y,z) = \partial_y[I(y,z)\cdot\partial_y\Phi(y,z)], \qquad \textbf{(11)}$$

relates the 3D intensity variation to the slope and curvature of the phase. A formal modification of Eq. (11) leads to

$$-2\pi\lambda_0^{-1}\text{dir}(\vec{S}) = \partial_y\Phi(y,z) \quad \text{with} \quad \text{dir}(\vec{S}) \equiv \partial y/\partial z, \qquad \textbf{(12)}$$

which accommodates the fact that the Poynting vector, characterized by its direction dir(.), is always oriented orthogonally to the local slope of the phase. In the frame of Monte-Carlo simulations, we interpret the measured intensity as a sorted set of rays which are statistically distributed according to the spatial probability distribution as defined via $I(y,z)$ in each detection plane and state two assumptions:

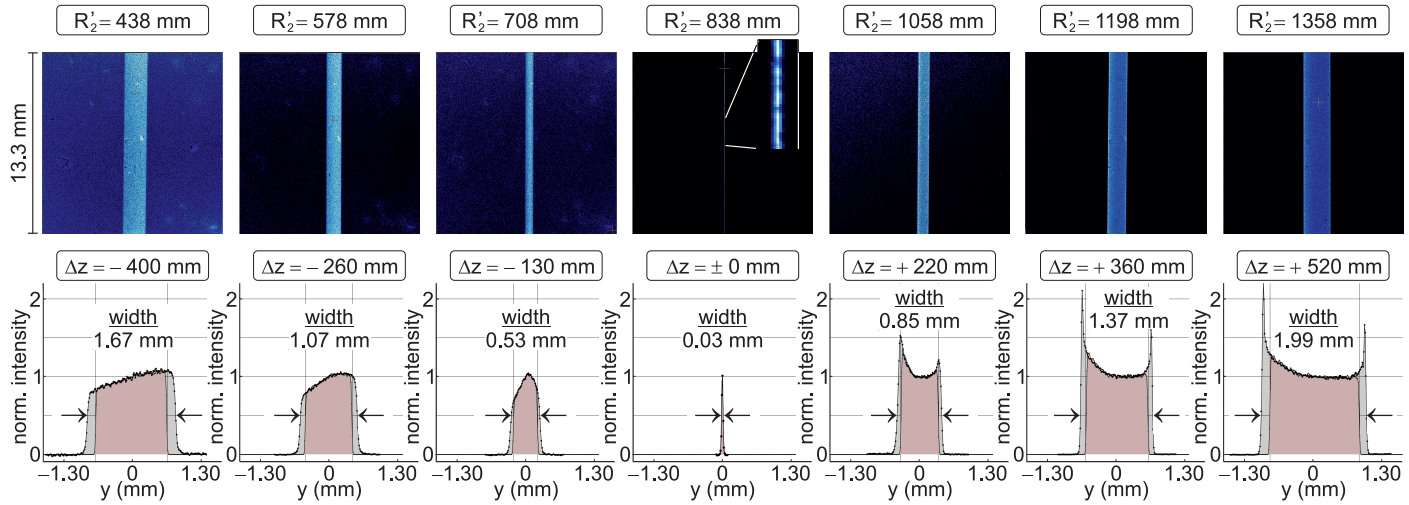

Fig. 8. Intensity distribution in the vicinity of the focal plane at $R_2^{'} = 838\,\text{mm}$, reflected from the spherical mirror "M_1". In the upper row, the images from the CCD camera are displayed, where the intensity increases with the brightness of blue tones. The lower row shows the measured (gray) and simulated (red) 1D intensity profile after tilt correction, background subtraction and normalization for the relative detector position $\Delta z \equiv R_2^{'} - 838\,\text{mm}$. All pictures are rotated by $-90°$ with respect to the coordinate system in Fig. 7.

• **Normalization:** Neglecting absorption along the free-space propagation in the evacuated system, the power $\int I(y,z)dy$ is maintained. For that purpose, the intensity as displayed in the 2nd row of Fig. 8 must be correspondingly re-normalized, to compensate fluctuations in the photon flux from the source.

• **No cross-over:** The small magnitude of wavefront aberrations and the lateral magnification of the beam cross section allow to neglect accidental cross-over rays for the trace from one detection plane to any other one – except from the focus which plays the role of an "intensity mirror" with respect to Δz.

Sequential ray tracing is performed for all "downstream" combinations of planes from Fig. 8, numbered from $1 \le i,j \le 7$, along the propagating beam: $i \to j$ with $j \ge i+1$ and $i,j \ne 4$. For each ray with index $1 \le n \le 10^7$ and coordinates $(y_n, \Delta z)$, the derivative from Eq. (12) is interpreted as

$$\partial y/\partial z \mapsto [\Delta z_j - \Delta z_i]^{-1}[y_{\pm n}(\Delta z_j) - y_n(\Delta z_i)], \qquad \textbf{(13)}$$

where the index "$+n$" refers to $i,j \le 3 \vee i,j \ge 5$ and "$-n$" denotes the cross-over case $i \le 3 \wedge j \ge 5$. For each one of the 15 sets $i \to j$, the numerical operation of Eqs. (12,13) yields, after integration along y and the free choice of an additive constant, the absolute phase as the sum of the dominant spherical term and a relatively small perturbation, in analogy to the additive separation of the mirror profile in Eq. (1). After the nonlinear fit and subtraction of those spheres, again in analogy to Eq. (2), the – as expected – similar phase functions for the 15 samples $i \mapsto j$ are

• **re-scaled** to the y-coordinates of the same observation plane, in our case the 1st one at $z_1 = 438\,\text{mm}$ or $\Delta z = -400\,\text{mm}$;
• arithmetically **averaged** to minimize statistical errors due to inaccuracies in the camera recordings and phase reconstruction.

In the chosen, fairly de-focused observation plane, the large cross section of the beam ensures an also wide-spread footprint on the grating substrate for the DWC, about 74 mm in the dispersive direction, which will be now designed in the HU mode with grazing angles $\alpha_0 = 2\theta/3$ and $\beta_0 = 4\theta/3$. Assuming that geometry, the reconstructed wavefront error $(2\pi)^{-1}\Phi(y,z_1)$ is

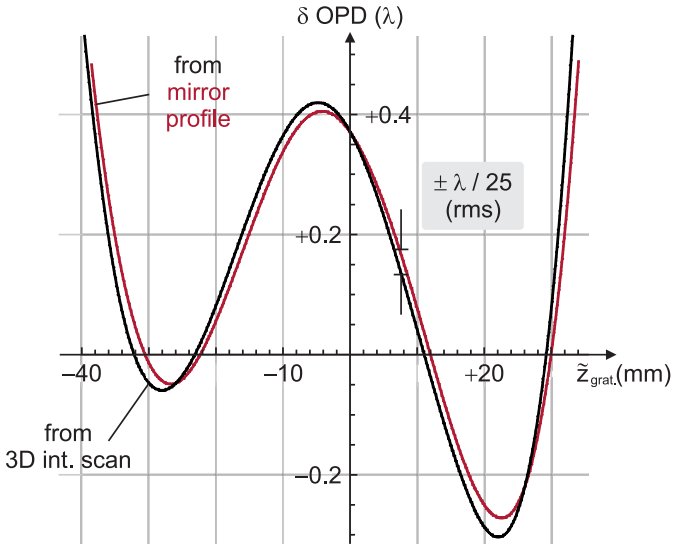

Fig. 9. Reconstructed wavefront distortion δ OPD from the ideal spherical shape in units of λ for the mirror "M_1" from Fig. 8, projected on the substrate plane (local coordinate $\tilde{z}_{\text{grat.}}$) of the DWC for the designed HU spectrometer. For comparison, the OPD as derived from the mirror profile is plotted in red.

projected on that plane, as shown in Fig. 9. The apparently good agreement with the reference from the mirror profile, calculated in the conventional scheme from Sect. 2, is quantified to a residual rms deviation of $\pm\lambda/25$ between the two curves. We simulate the performance of the HU spectrometer with (subscript "DWC") and without correction ("RZP") of the reconstructed wavefront error and find a focal spot size of

$$\varnothing_{\text{RZP}}^{(\text{foc})} = 4.39\,\mu\text{m} \quad \text{and} \quad \varnothing_{\text{DWC}}^{(\text{foc})} = 1.06\,\mu\text{m}, \qquad \textbf{(14)}$$

respectively. The phase retrieval thus improves the resolution by a factor of 4.2, where the diffraction limit $(0.65\,\mu\text{m})$ is nonetheless still exceeded by 64 % in the DWC version, mainly caused by the slight but systematic shift in the lateral $\tilde{z}_{\text{grat.}}$-direction (see

Fig. 9) that occurred in nearly all 15 sample calculations from above. Though the wavefront reconstruction from 3D intensity scans presently does not work as precise as the direct calculation from the mirror's surface, future technical improvements in that method might yield refined results of competitive accuracy.

4. INTEGRATED OPTICS USING MIRROR PROFILES

Alternatively to the *in situ* and "at wavelength" phase detection as applied in Sect. 3, the form and figure errors of the collecting mirror with its common toroidal profile can be measured *ex situ* as well: In the case of sufficiently large meridional (M) and sagittal (S) radii of curvature $R_{M,S} \gtrsim 10\,\mathrm{m}$, the LTP can provide the required information, as used for validation in Sect. 3.

To incorporate the transverse slope in the $x-$direction, and especially to characterize highly curved substrates [33] with $R_{M,S} \gtrsim 1\,\mathrm{m}$, a newly developed method uses a differential interferometer (SIOS SP-DIS series), enabling true 3D mapping with 0.1 nm resolution, as sketched in Fig. 10. During a measurement, the mirror under test and a reference mirror are statically fixed in the setup. The interferometer is moved in a x-z scan while it detects the y distance variations between the mirrors. By subtracting the form deviations of the reference mirror from the measurements, the y-topography of the mirror under test is determined. Due to the principle of the interferometer, y-motion errors of the scanning stage do not affect the measurements. The interferometer beam is focused with a standard convex lens onto the mirror under test. Therefore, in contrast to known Fizeau interferometer setups, also curved and sloped mirrors can be measured without the need for expensive spherical reference optics with respective radii. Due to the focused interferometer beam, the lateral resolution is $\sim 10\,\mu$m. In first investigations, a commercially available [27], spherical mirror "M_2" of length L and width W with a large radius of curvature (ROC) was measured, as specified in Tab. 3. The substrate thickness $\Delta t_{\mathrm{sub.}}$

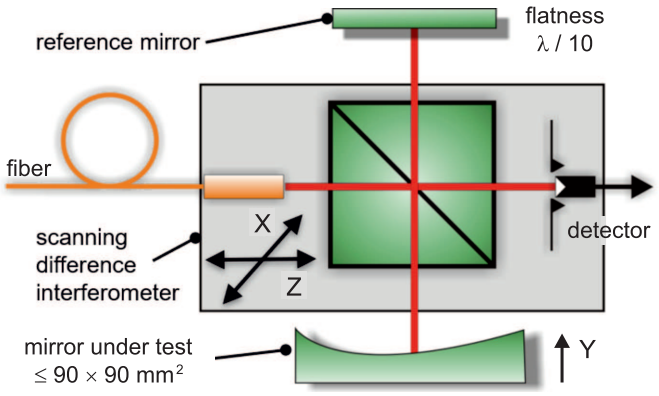

Fig. 10. Scheme of the interferometric setup "SP-DIS" at SIOS GmbH. A fiber-coupled HeNe laser $(\lambda = 632.8\,\mathrm{nm})$ beam (red) is used at the beamsplitter cube with a flat reference to test the curved mirror profile $y(x,z)$. The focusing unit is not drawn.

Table 3. Technical specifications of the mirror sample "M_2"

size $(L \times W)$	$\Delta t_{\mathrm{sub.}}$	ROC	surface	$\pm\sigma$ (rms)
$100 \times 30\,\mathrm{mm}^2$	8 mm	28.62 m	blank Si	$\approx 0.25\,\mathrm{nm}$

ensures sufficient mechanical stability to avoid deformations due to gravitation and / or tension in the sample holder. On the other hand, diffuse scattering is not relevant at all in the soft X-ray regime [3, 34] for the super-polished surface with a micro-roughness on the Angstrom scale. Figure 11 shows on the left the profile data, as obtained by means of the differential interferometer from Fig. 10. A repeatability of the measured

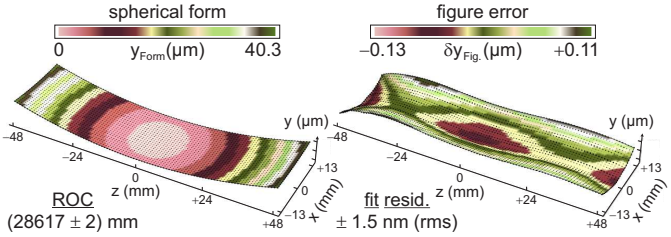

Fig. 11. Profile of the sphere "M_2", according to Tab. 3. Raw 3D data $y_i(x_i, z_i)$ (black dots) are measured on a regular grid of 97×27 points with a sampling distance of 1 mm and fitted by a sphere (left). The figure error is separated and modeled with a polynomial of 20$^{\mathrm{th}}$ order (right). Both shapes are color-coded as well as characterized by the ROC and fit residuals.

y-topography of $< 2\,\mathrm{nm}$ at specific x-z locations on the mirror can be achieved. The data $y_i(x_i, z_i)$ feature thus a high reliability, and the radius of curvature is evaluated to $R_{M,S} = 28617\,\mathrm{mm}$ by means of the model in Eq. (2) with an uncertainty of $\pm 7 \times 10^{-5}$ or less than $\pm 2\,\mathrm{mm}$. Following the concept from Eq. (1), the figure error is separated and its polynomial fit approximates the data residuals to an accuracy of $\pm 5.0\,\mathrm{nm}$ (P-V) or $\pm 1.5\,\mathrm{nm}$ (rms), respectively. The results are depicted in Fig. 11 on the right.

Such an assembly allows to build a compact soft X-ray spectrometer in an evacuated housing. In particular, we want to analyze the fluorescence spectrum of a TiO_2 target around the Ti L$\beta_{1,6}$ doublet [26] near 0.5 keV. Entrance and exit arm lengths $R'_{1,2}$ are listed in Tab. 4, together with the associated angles α_0 and β_0. The mean angular acceptance $\langle \Delta\vartheta \rangle_{\mathrm{H,V}}$, as also sketched

Table 4. Design parameters of the example Ti spectrometer

E_0	R'_1	R'_2	α_0	β_0	$\langle \Delta\vartheta \rangle_{\mathrm{H,V}}$
458.6 eV	838 mm	2500 mm	2.59°	4.11°	4.8 mrad

in Fig. 12, corresponds to an illuminated aperture of at least $4 \times 80\,\mathrm{mm}^2$ on the mirror – i.e. the structured grating field. This restriction to a relatively narrow strip helps – on the one

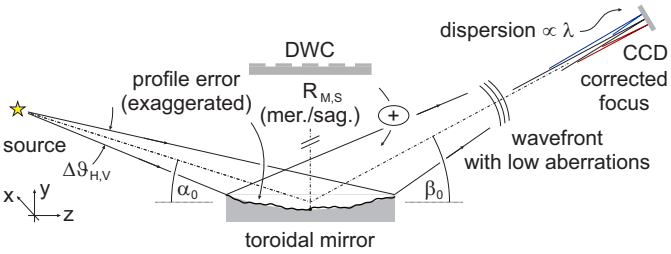

Fig. 12. The idea of an all-in-one reflective-diffractive optical element, which contains the customized DWC directly inscribed into the toroidal mirror substrate with meridional / sagittal radii of curvature and the evaluated profile error.

hand – to limit the line density at the edges for the aimed 2D focusing DWCs and enables – on the other hand – writing of several, parallel grating structures on the same substrate, e.g. for variable target materials and experimental conditions.

The calculation of the groove structure for the DWC follows, in principle, the procedure from Sect. 2. Unlike the sequential, usually ray-traced combination of the two optical elements in the HU scheme however, their integration to an all-in-one component allows an elegant, clearly arranged formulation of the defining relation for the phase $\Phi(x,z)$. We find

$$(2\pi/\lambda_0)^{-1}\Phi(x,z) + (R_1^{'} + R_2^{'}) = \mathcal{F}_1(x,z) + \mathcal{F}_2(x,z). \quad \textbf{(15)}$$

The auxiliary functions $\mathcal{F}_{1,2}(x,z)$ in Eq. (15) describe the optical path length in analogy to an ordinary RZP on a plane substrate [14, 16], but now for an arbitrary profile $y_M(x,z)$ in still analytical terms, i.e.

$$\mathcal{F}_1(x,z) = \sqrt{x^2 + [z + R_1\cos\theta]^2 + [y_M(x,z) - R_1\sin\theta]^2},$$
$$\mathcal{F}_2(x,z) = \sqrt{x^2 + [z - R_2\cos\theta]^2 + [y_M(x,z) - R_2\sin\theta]^2}.$$

As an off-axis grating segment, necessary for the exclusion of the specular reflection from the detector plane [14], the DWC is characterized in Eq. (15) by arm lengths $R_{1,2}$ and the reflection angle θ. These quantities are related to the constructive parameters from Tab. 4 via $(R_1 + R_2)\cos\theta = R_1^{'}\cos\alpha_0 + R_2^{'}\cos\beta_0$, in combination with $R_1\sin\theta = R_1^{'}\sin\alpha_0$ and $R_2\sin\theta = R_2^{'}\sin\beta_0$. Equipped with the complete information on the instrumental geometry, the expression for the phase from Eq. (15) serves as the input for the condition in Eq. (6), and the Fresnel zones can be computed "point by point" using an appropriate code in Mathematica™ or Python [33], for instance. Figure 13 depicts in the upper row the overall appearance of the DWC. The regular RZP, which corrects only for the spherical form but not the figure error, is drawn in the lower row for comparison. Obviously, both versions look indistinguishable with the naked eye. Their difference on the microscopic scale however, depicted for selected lines in the central row of Fig. 13, decides on the spatial and spectral resolution that can be achieved under otherwise optimal conditions presumed as follows:

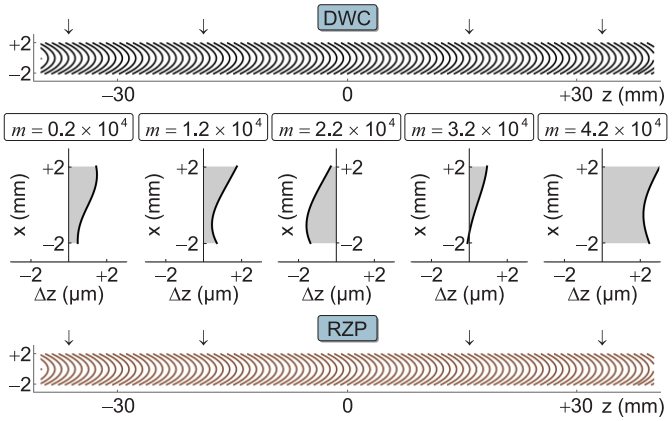

Fig. 13. Comparison of the grating line structures for the DWC (top) and RZP (bottom), written on the mirror "M_2" from Fig. 11. Each 500$^{\text{th}}$ line is drawn for simplicity. The deviations $\Delta z(x)$ are displayed for a series of line numbers m along the grating aperture (indicated by arrows) in the central row. Note the different length units [μm] vs. [mm] in this zoomed plot.

• **Source:** An ideal point source cannot be realized in practice. Nevertheless, spatial coherence is also provided in case of a sufficiently plane wavefront for the incident beam, e.g. at certain synchrotron beamlines or free-electron laser (FEL) facilities. The grating structure has to be modified, i.e. designed for an infinite entrance arm length $R_1^{'} \to \infty$.

• **Detector:** The real detector with its constraints is omitted in the calculation. To reach the maximum performance, the spatial resolution element of the camera etc. should not exceed the width of the diffraction-limited point spread function (PSF), in the present example determined to $\varnothing_{\text{PSF}} = 1.2\,\mu$m.

• **Adjustment:** Misalignment plays a minor role for state-of-the-art positioning mechanics and can be neglected, in particular for the all-in-one configuration as considered in this Sect. 4.

Given those three prerequisites, the camera image of the modeled source spectrum [26] may be simulated using Monte-Carlo routines [35]. The reflectivity of the Si mirror varies only slightly across the considered energy range, within $(76.3 - 77.5)$ % [36], and is thus approximated as a constant. Caused by the spherical mirror shape, the raw ray tracing data yield slightly curved, rather than straight intensity distributions in the detector plane. After linearization to horizontal focal lines by an ordinary fitting procedure, the atomic peaks are finally convolved with the PSF. Figure 14 shows the result for the TiO_2 spectrum.

From the doublet around 0.40 keV to the high energy end near 0.53 keV, the height of the peaks varies by about an order of magnitude, due to the energy-dependent efficiency of the photon creation process in the target material [26]. Like in the HU scheme as characterized by Fig. 5, the wide-range behavior of the resolving power may be classified in two regimes:

• **Figure error compensation:** The width of the sharp spectral lines in the vicinity of E_0 from Tab. 4 can be ascribed to the wavefront correction by the customized DWC, rather than the "regular" RZP (Fig. 13). Correspondingly, the resolving power $E/\Delta E$ increases from 2.6×10^4 for Ti Lα, Lγ to the theoretical maximum of 4.5×10^4 for the central Ti L$\beta_{1,6}$ doublet.

• **Curved substrate effect:** An effective suppression of aberrations toward the outer regions of the spectrum is accomplished by the spherical shape of the mirror in which the grating is inscribed [33]. In contrast, the relative bandwidth of an RZP on a plane substrate would be typically restricted to a few % around E_0. The mean resolving power for the Ti and O peaks around 0.40 keV and 0.53 keV, respectively, is estimated to $\approx (7 \pm 2) \times 10^3$. The coma tails, which are visible on the left and right in Fig. 14, affect the result notably, and special cutoff techniques might be applied to the low intensity level [37] to control both photon flux and resolution in these spectral lines.

We compare the resolution at E_0 for the uncorrected (RZP) with the corrected (DWC) grating from Fig. 13, under otherwise identical conditions and the three assumptions for an optimized instrumental arrangement from above,

$$(E/\Delta E)_{\text{RZP}} = 2.76 \times 10^3 \quad \text{vs.} \quad (E/\Delta E)_{\text{DWC}} = 4.49 \times 10^4. \quad \textbf{(16)}$$

If we take the number of illuminated grating lines as the analytical maximum for the possible resolving power, the DWC as designed and simulated here in Sect. 4 should reach 98 % of that benchmark, i.e. the diffraction limit. In most practical implementations of course, the more or less serious "violation" of the three idealizing items will reduce the quality of the spectrometer accordingly, and the real performance may be calculated

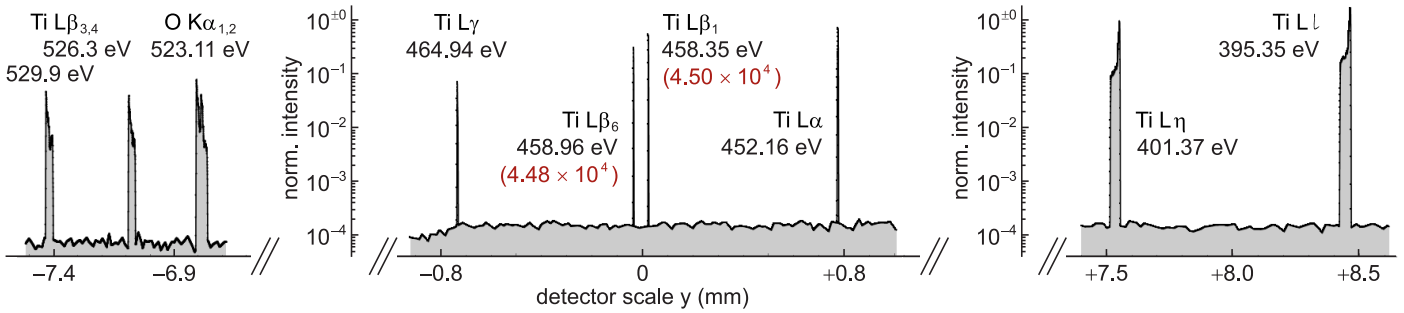

Fig. 14. Simulated TiO_2 spectrum, recorded using the DWC-structured mirror from Fig. 11 for a point source and an ideal detector with unlimited spatial resolution. All referenced emission lines [26] in the range from 395 eV to 529 eV are sampled with a resolution of 1.2 μm, whereas an about 15-fold larger step size is used for the bremsstrahlung continuum [26]. The intensity is normalized to the maximum (Ti L l) and the red numbers in brackets indicate the theoretical resolving power for the central $L\beta_{1,6}$ doublet.

easily considering the geometrical magnification of the source, the convolution with the detector resolution and error budget simulations for any potential alignment tolerance.

5. CONCLUSION

In this paper, we elaborate a simple, geometrical theory of diffractive wavefront correction for grating-based optical instrumentation in the XUV and soft X-ray regime, as well as initial steps toward its experimental realization. Our findings prove that a customized DOE can compensate the wavefront deformation as it is induced by the usually inevitable form and figure error of the collecting mirror, enabling diffraction-limited resolution near the design energy and, beyond, wide-range wavelength-dispersive spectroscopy as well. Such gratings with an exact, "holographic" line density distribution are calculated in three dimensions for various configurations, e.g. the common Hettrick-Underwood scheme or an especially compact, easily aligned and highly efficient integrated design. The two-dimensional groove structure can be directly inscribed into any plane or curved substrate.

The successful design relies on an accurate knowledge of the wavefront that emerges from the erroneous mirror. Two methods are presented: The standard way to generate the DWC for a given setup utilizes the new technology for ultra-precise, Angstrom-scaled profile measurement of highly curved mirrors as developed by SIOS GmbH in the framework of this project. With radii of curvature down to $\gtrsim$ m on mirror apertures up to $90 \times 90\,\mathrm{mm}^2$, compact table-top spectrometers with an unprecedented performance may be constructed [33]. Here, we demonstrate the potential with an in-house experiment for TiO_2 spectroscopy across an energy range of $(0.39 - 0.53)$ keV with a resolving power $E/\Delta E$ up to 4.5×10^4. Detailed modeling and simulation quantify the gain in $E/\Delta E$ to one order of magnitude, due to the incorporation of the mirror's figure error with an amplitude of only ± 31 nm. A complementary approach evaluates the phase map of the outgoing beam directly, by a 3D scan of its intensity distribution in multiple intra- and extra-focal detection planes. A relatively tolerant, i.e. stable phase retrieval algorithm for the fairly incoherent source is developed from the 1D transport-of-intensity equation and the reconstruction works up to an accuracy of $\pm\lambda/25$ (rms) so far – with room for more.

Subsequently, the explicit computation of the DWC structure is – compared to the initial, Mathematica™-based code being used for the present study – vastly accelerated to typically $\lesssim$ 10 min by means of an already available Python routine [33]. Beyond the diverse methods as discussed within this work, software-oriented deep learning using neural nets could promise, in future, highest reliability for use in rough environments with partially incoherent beams and omnipresent noise [38, 39].

On the roadmap toward a potential routine for not only easily calculated but also quickly produced DWC gratings, there is likely no way around the benefits of modern nano-fabrication methods. Above all, the emerging technique of direct laser writing [40, 41] is expected to allow for an inexpensive generation of true 3D VLS groove patterns, at least for the relatively relaxed line densities in the XUV and soft X-ray regime.

Until now, we investigated the diffractive wavefront correction for the class of laboratory-sized spectrometers in the XUV and soft X-ray regime. Nevertheless, the basic theoretical concepts from Sect. 2 and the practical techniques (Sects. 3,4) can be applied as well to large-scale instruments at synchrotron or FEL facilities [22–25], and are – in principle – scalable to any, especially short wavelengths in the hard X-ray range.

In view of laser-driven high harmonic generators (HHGs) and other, modern laboratory-scaled sources at about 1000 universities and research institutes worldwide, as well as more than 50 synchrotron facilities with at least one mirror-based soft X-ray beamline, we may expect a significant request for DWC optics in the future, yielding "low budget" spectroscopy on a level of high scientific performance.

FUNDING INFORMATION

European Fund for Regional Development (EFRE) project REFLEX (10162889) by the German Federal Ministry for Economic Affairs and Energy (ZF4303901GR6, VaLiS) and (ZF4303901GR6, NeuGaR).

ACKNOWLEDGMENTS

The authors thank all colleagues from IAP e.V., NOB GmbH, BESSY II and other institutions for inspiring discussions, beside their kind technical and administrative support.

REFERENCES

1. M. C. Hettrick, J. H. Underwood, P. J. Batson, and M. J. Eckart, "Resolving power of 35,000 (5 mA) in the extreme ultraviolet employing a grazing incidence spectrometer," Appl. Opt. **27**, 200 – 202 (1988).
2. V. N. Strocov, T. Schmitt, U. Flechsig, L. Patthey, and G. S. Chiuzbăian, "Numerical optimization of spherical variable-line-spacing grating X-ray spectrometers," J. Synchrotron Rad. **18**, 134 – 142 (2011).

3. T. Pardini, D. Cocco, and S. P. Hau-Riege, "Effect of slope errors on the performance of mirrors for x-ray free electron laser applications," Opt. Express **23**, 31889 – 31895 (2015).
4. A. Sakdinawat and D. Attwood, "Nanoscale X-ray imaging," Nat. Photonics **4**, 840 – 848 (2010).
5. G. E. Ice, J. D. Budai, and J. W. L. Pang, "The Race to X-ray Microbeam and Nanobeam Science," Science **334**, 1234 – 1239 (2011).
6. J. C. da Silva, A. Pacureanu, Y. Yang, S. Bohic, C. Morawe, R. Barrett, and P. Cloetens, "Efficient concentration of high-energy x-rays for diffraction-limited imaging resolution," Optica **4**, 492 – 495 (2017).
7. S. Matsuyama, I. Inoue, J. Yamada, J. Kim, H. Yumoto, Y. Inubushi, T. Osaka, I. Inoue, T. Koyama, K. Tono, H. Ohashi, M. Yabashi, T. Ishikawa, and K. Yamauchi, "Nanofocusing of X-ray free-electron laser using wavefront-corrected multilayer focusing mirrors," Sci. Rep. **8**, 17440 (2018).
8. H. Mimura, S. Handa, T. Kimura, H. Yumoto, D. Yamakawa, H. Yokoyama, S. Matsuyama, K. Inagaki, K. Yamamura, Y. Sano, K. Tamasaku, Y. Nishino, M. Yabashi, T. Ishikawa, and K. Yamauchi, "Breaking the 10 nm barrier in hard-X-ray focusing," Nat. Phys. **6**, 122 – 125 (2010).
9. F. Yang, M. Li, L. Gao, W. Sheng, P. Liu, and X. Zhang, "Laser-heating-based active optics for synchrotron radiation applications ," Opt. Lett. **41**, 2815 – 2818 (2016).
10. K. Sawhney, D. Laundy, V. Dhamgaye, and I. Pape, "Compensation of X-ray mirror shape-errors using refractive optics," Appl. Phys. Lett. **109**, 051904 (2016).
11. F. Seiboth, A. Schropp, M. Scholz, F. Wittwer, C. Rödel, M. Wünsche, T. Ullsperger, S. Nolte, J. Rahomäki, K. Parfeniukas, S. Giakoumidis, U. Vogt, U. Wagner, C. Rau, U. Boesenberg, J. Garrevoet, G. Falkenberg, E. C. Galtier, H. J. Lee, B. Nagler, and C. G. Schroer, "Perfect X-ray focusing via fitting corrective glasses to aberrated optics," Nat. Commun. **8**, 14623 (2017).
12. D. Cojoc, E. Ferrari, V. Garbin, S. Cabrini, A. Carpentiero, M. Prasciolu, L. Businaro, B. Kaulich, and E. Di Fabrizio, "Wave front engineering by means of diffractive optical elements, for applications in microscopy," Proc. SPIE **6254**, 625416 (2006).
13. R. Liu, F. Li, M. J. Padgett, and D. B. Phillips, "Generalized photon sieves: fine control of complex fields with simple pinhole arrays," Optica **2**, 1028 – 1036 (2015).
14. M. Brzhezinskaya, A. Firsov, K. Holldack, T. Kachel, R. Mitzner, N. Pontius, J.-S. Schmidt, M. Sperling, C. Stamm, A. Föhlisch, and A. Erko, "A novel monochromator for experiments with ultrashort X-ray pulses," J. Synchrotron Rad. **20**, 522 – 530 (2013).
15. J. Metje, M. Borgwardt, A. Moguilevski, A. Kothe, N. Engel, M. Wilke, R. Al-Obaidi, D. Tolksdorf, A. Firsov, M. Brzhezinskaya, A. Erko, I. Y. Kiyan, and E. F. Aziz, "Monochromatization of femtosecond XUV light pulses with the use of reflection zone plates," Opt. Express **22**, 10747 – 10760 (2014).
16. C. Braig, H. Löchel, R. Mitzner, W. Quevedo, P. Loukas, M. Kubin, C. Weniger, A. Firsov, J. Rehanek, M. Brzhezinskaya, P. Wernet, A. Föhlisch, and A. Erko, "Design and optimization of a parallel spectrometer for ultra-fast X-ray science," Opt. Express **22**, 12583 – 12602 (2014).
17. H. Löchel, C. Braig, M. Brzhezinskaya, F. Siewert, P. Baumgärtel, A. Firsov, and A. Erko, "Femtosecond high-resolution hard X-ray spectroscopy using reflection zone plates," Opt. Express **23**, 8788 – 8799 (2015).
18. J. E. Harvey and C. L. Vernold, "Description of Diffraction Grating Behavior in Direction Cosine Space," Appl. Opt. **37**, 8158 – 8160 (1998).
19. P. Baumgärtel, P. Grundmann, T. Zeschke, A. Erko, J. Viefhaus, F. Schäfers, and H. Schirmacher, "RAY-UI: New Features and Extensions," AIP Conf. Proc. **2054**, 060034 (2019).
20. E. Muslimov, E. Hugot, W. Jahn, S. Vives, M. Ferrari, B. Chambion, D. Henry, and C. Gaschet, "Combining freeform optics and curved detectors for wide field imaging: a polynomial approach over squared aperture," Opt. Express **25**, 14598 – 14610 (2017).
21. O. Fuchs, L. Weinhardt, M. Blum, M. Weigand, E. Umbach, M. Bär, C. Heske, J. Denlinger, Y.-D. Chuang, W. McKinney, Z. Hussain, E. Gullikson, M. Jones, P. Batson, B. Nelles, and R. Follath, "High-resolution, high-transmission soft x-ray spectrometer for the study of biological samples," Rev. Sci. Instrum. **80**, 063103 (2009).
22. S. Rutishauser, L. Samoylova, J. Krzywinski, O. Bunk, J. Grünert, H. Sinn, M. Cammarata, D. M. Fritz, and C. David, "Exploring the wavefront of hard X-ray free-electron laser radiation," Nat. Commun. **3**, 947 (2012).
23. S. Dziarzhytski, N. Gerasimova, R. Goderich, T. Mey, R. Reininger, M. Rübhausen, F. Siewert, H. Weigelt, and G. Brenner, "Microfocusing at the PG1 beamline at FLASH," J. Synchrotron Rad. **23**, 123 – 131 (2016).
24. Y. Liu, M. Seaberg, D. Zhu, J. Krzywinski, F. Seiboth, C. Hardin, D. Cocco, A. Aquila, B. Nagler, H. J. Lee, S. Boutet, Y. Feng, Y. Ding, G. Marcus, and A. Sakdinawat, "High-accuracy wavefront sensing for x-ray free electron lasers," Optica **5**, 967 – 975 (2018).
25. M. Seaberg, R. Cojocaru, S. Berujon, E. Ziegler, A. Jaggi, J. Krempasky, F. Seiboth, A. Aquila, Y. Liu, A. Sakdinawat, H. J. Lee, U. Flechsig, L. Patthey, F. Koch, G. Seniutinas, C. David, D. Zhu, L. Mikes, M. Makita, T. Koyama, A. P. Mancuso, H. Chapman, and P. Vagovič, "Wavefront sensing at X-ray free-electron lasers," J. Synchrotron Rad. **26**, 1 – 12 (2019).
26. F. Salvat, "PENELOPE-2014: A Code System for Monte-Carlo Simulation of Electron and Photon Transport," Univ. de Barcelona, Spain, http://www.oecd-nea.org (2015).
27. Pilz-Optics, Enzianstr. 29, 73485 Zöbingen-Unterschneidheim, Germany, http://www.pilz-optics.de (2019).
28. F. Siewert, J. Buchheim, S. Boutet, G. J. Williams, P. A. Montanez, J. Krzywinski, and R. Signorato, "Ultra-precise characterization of LCLS hard X-ray focusing mirrors by high resolution slope measuring deflectometry," Opt. Express **20**, 4525 – 4536 (2012).
29. F. Siewert, "Metrology, Mirrors and Gratings – Advances and Challenges in Synchrotron Optics," J. Phys. Conf. Ser. **425**, 152001 (2013).
30. G. Pedrini, W. Osten, and Y. Zhang, "Wave-front reconstruction from a sequence of interferograms recorded at different planes," Opt. Lett. **30**, 833 – 835 (2005).
31. M. R. Teague, "Deterministic phase retrieval: a Green's function solution," J. Opt. Soc. Am. **73**, 1434 – 1441 (1983).
32. J. C. Petruccelli, L. Tian, and G. Barbastathis, "The transport of intensity equation for optical path length recovery using partially coherent illumination," Opt. Express **21**, 14430 – 14441 (2013).
33. C. Braig, J. Probst, E. Langlotz, I. Rahneberg, M. Kühnel, A. Erko, T. Krist, and C. Seifert, "Diffraction compensation of slope errors on strongly curved grating substrates," Proc. SPIE **11109**, 111090U (2019).
34. B. Aschenbach, "Boundary between geometric and wave optical treatment of X-ray mirrors," Proc. SPIE **5900**, 59000D (2005).
35. Optica Software, 4679 Torrey Circle #204, San Diego, CA 92130, USA, http://www.opticasoftware.com (2019).
36. B. L. Henke, E. M. Gullikson, and J. C. Davis, "X-ray interactions: photoabsorption, scattering, transmission, and reflection at E=50-30000 eV, Z=1-92," Atomic Data and Nuclear Data Tables **54**, 181 – 342 (1993).
37. Z. Yin, J. Rehanek, H. Löchel, C. Braig, J. Buck, A. Firsov, J. Viefhaus, A. Erko, and S. Techert, "Highly efficient soft X-ray spectrometer based on a reflection zone plate for resonant inelastic X-ray scattering measurements," Opt. Express **25**, 10984 – 10996 (2017).
38. Y. Rivenson, Y. Zhang, H. Günaydin, D. Teng, and A. Ozcan, "Phase recovery and holographic image reconstruction using deep learning in neural networks," Light-Sci. Appl. **7**, 17141 (2018).
39. Y. Nishizaki, M. Valdivia, R. Horisaki, K. Kitaguchi, M. Saito, J. Tanida, and E. Vera, "Deep learning wavefront sensing," Opt. Express **27**, 240 – 251 (2019).
40. T. Gissibl, S. Thiele, A. Herkommer, and H. Giessen, "Two-photon direct laser writing of ultracompact multi-lens objectives," Nat. Photonics **10**, 554 – 560 (2016).
41. U. T. Sanli, H. Ceylan, I. Bykova, M. Weigand, M. Sitti, G. Schütz, and K. Keskinbora, "3D Nanoprinted Plastic Kinoform X-Ray Optics," Adv. Mater. **30**, 1802503 (2018).